Case Studies in Construction Materials 18 (2023) e01945

Contents lists available at ScienceDirect

Case Studies in Construction Materials

journal homepage: www.elsevier.com/locate/cscm

Case study

Towards development of sustainable lightweight 3D printed wall building envelopes – Experimental and numerical studies

Karla Cuevas [a], Jarosław Strzałkowski [b], Ji-Su Kim [c], Clemens Ehm [a], Theresa Glotz [d], Mehdi Chougan [e], Seyed Hamidreza Ghaffar [e,f], Dietmar Stephan [a,*], Pawel Sikora [a,b,*]

[a] Building Materials and Construction Chemistry, Technische Universität Berlin, Germany
[b] Faculty of Civil and Environmental Engineering, West Pomeranian University of Technology in Szczecin, Poland
[c] Department of Civil Engineering, University of Seoul, South Korea
[d] Structural Mechanics, Technische Universität Berlin, Germany
[e] Department of Civil and Environmental Engineering, Brunel University London, Uxbridge UB8 3PH, United Kingdom
[f] Applied Science Research Center, Applied Science Private University, Jordan

ARTICLE INFO

Keywords:
3D printing
Lightweight concrete
Wall
Thermal insulation
Building envelope

ABSTRACT

3D printing technology can be of crucial importance in the design of sustainable and energy-efficient building envelopes. With this technology, there is the potential to mechanically and thermally optimise the topology of printed walls. Additionally, the printing and infill materials used can be insulating, and thus contributing to the overall reduction of heat loss. To date, limited examples of 3D printed envelopes and information about the thermal and mechanical performance of 3D printed walls are available. This study developed a 3D printable wall element with an insulating property for application in building envelopes. Seven wall topologies are studied through simulations of mechanical and thermal performance using two mixtures: a control mixture (normal-weight) and a lightweight mixture containing expanded thermoplastic microspheres (ETM) for thermal insulation. One wall topology is selected based on the performance of the simulation and printed using both mixtures. The 3D printed envelopes were tested under compressive strength and analysed with the ARAMIS system, a digital image correlation (DIC) technology. Computer simulations and the DIC analysis identified the main causes for failure, which are the inter-filament weakness and the imperfections of the geometry of the printed envelope.

1. Introduction

3D printable cementitious composites have been studied as alternate means of constructing concrete structures, prompted by current breakthroughs in additive manufacturing technology [1]. This novel building method has the ability to address several essential issues in the present construction industry in terms of eliminating the need for temporary formwork and vibrations, both commonly used in concreting, are no longer required [2]. Moreover, digital fabrication of concrete exhibited a strong potential to

* Correspondence to: Building Materials and Construction Chemistry, Technische Universität Berlin, Gustav-Meyer-Allee 25, 13355 Berlin, Germany.
E-mail addresses: stephan@tu-berlin.de (D. Stephan), pawel.sikora@zut.edu.pl (P. Sikora).

https://doi.org/10.1016/j.cscm.2023.e01945
Received 22 December 2022; Received in revised form 16 February 2023; Accepted 20 February 2023
Available online 21 February 2023

incorporate high amount of fine waste and/or by-product materials in their mixture compositions [3,4]. As a result, 3D printing as an automated building approach can diminish greenhouse gas (GHG) emissions, resource demands, raw material waste, construction time, and human errors in the formwork construction process [5]. Furthermore, it enables a novel approach to concrete design in which the material and components are parametrically developed to achieve the best structural performance and functions [6]. One of the fields in the building industry where concrete 3D printing can play a significant role is associated with the production of lightweight structures. Lightweight coarse aggregate (LWA) alternatives, including expanded perlite [7], shale [8], and dry-expanded thermoplastic microsphere [9], have been used in conventional lightweight concrete (LWC). LWC is widely recognised as suitable material given its lower density, adequate strength, and excellent thermal and acoustic insulation [10–12]. These parameters are important both to meet the technical requirements to be used in high-rise buildings and to produce thermally efficient building envelopes.

Research conducted by Robati et al. [13] explored the correlation between mix formulation and the resulting thermal efficiency of the produced concrete 3D printed objects. Their results confirmed that the mix formulation, specifically the aggregate's density and materials proportion, substantially impacts the thermal efficiency of 3D printed objects. Similar results have been reported in other studies, in which the material characteristics and density of the 3D printing mortar directly impact the thermal insulating efficacy of the 3D printed elements [14,15]. In low-density mortars, mechanical strength loss is unavoidable [16,17]. However, rapid action is required to improve the thermal insulation of building envelopes and reduce overall energy consumption for heating as per the European Energy Efficiency Directive objective for climate neutrality of building stock by 2050 [18]. For instance, in a study conducted by Weger et al. [19], particle bed 3D printing was employed to construct lightweight 3D printed concrete in which reductions of 3.5–4.4 times were recorded in the lightweight sample's thermal conductivity and up to 2 times in mechanical performance. Owing to 3D printing structural self-weight can be reduced by optimising the mixture design, introducing low thermal conductive materials, and optimising the architectural parameters of printed elements [20]. Moreover, life cycle assessment (LCA) study suggested that 3D printing with lightweight concrete materials can decrease negative impacts on the environment compared with the printing of normal-weight materials later down the life cycle, particularly in the operational phase [21].

Although LWC technology is well-developed, systematic investigations on the preparation and manufacturing of lightweight concrete are lacking. In this regard, Wang et al. [20] evaluated the mechanical behaviours of 3D printed concrete structures of sizes $100 \cdot 100 \cdot 400\ mm^3$ and $150 \cdot 150 \cdot 150\ mm^3$ with hollow sections. Fine sand has been replaced up to 30 wt% with ceramsite sand to decrease the density of the elements. Structures with different topologies were evaluated, showing the promising approach for using 3D printing technology. However, no data on the thermal characteristics of the proposed structures were available. Some researchers have attempted to optimise the thermal efficiency of 3D printed objects via geometry optimisation approaches [22,23]. Research conducted by Buswell et al. [23] compared two wall panels with identical exterior geometry but different internal cross-section printing paths, aiming to increase the thermal insulation of 3D printed wall elements. Their proposed strategy implies that designing cavities with varying levels of thermal performance in sections that demand high thermal resistivity can enhance insulating characteristics. It is worth noting that the thermal efficiency of a 3D printed wall, and consequently the design of wall geometry, also dependents on the type and characteristics of the printing materials. The thermal performance of 3D printed cavity walls using two categories of cementitious composite feedstocks (i.e., fibre-reinforced high-performance concrete and lightweight foam concrete) confirmed the presence of cavities in the high-performance concrete wall, which has high thermal conductivity, and therefore enhanced its thermal performance by nearly 1 °C.

In contrast, employing lightweight foam concrete (i.e., low thermally conductive material) in an identical cavity configuration has diminished thermal performance by almost 1 °C [24]. Apart from the studies above, attempts to develop 3D-printed hollow structures using lightweight concrete are limited. Waste glass has received a particular interest in conventional concrete technology as, despite its low thermal conductivity, it exhibits good mechanical properties attributed to the mechanical interlocking of elongated and needle-shaped grains obtained during the grinding process [25]. This, in turn, could affect the fresh characteristics of concrete. The fresh properties (e.g., printability) of lightweight concrete incorporating lightweight expanded clay aggregates (LECA) were investigated by Rahul and Santhanam [26], and enhancements in the strength and elastic modulus of concrete in its fresh state were evidenced.

Although recent research shows that lightweight concrete can lower self-weight and thermal conductivity in 3D printing, they mainly highlighted employing the lightweight concrete mix for 3D printing. Yet, no systematic research has been performed on the 3D printing of lightweight structures that consider stress distribution and thermal insulation optimisation utilising different printing pathways.

This work aims to develop a printable wall element with an insulating ability for application in building envelopes. The lightweight mixture designed in the authors' previous study was employed as a source mixture used for the 3D printing of the wall [27], and selected data were taken as input data for thermal simulations. Afterwards, a set of printing topology variations were simulated to find out the optimised building envelope topology. In the final state, a selected variant of the wall element was printed and verified through numerical and destructive testing, proving the possibility of developing lightweight wall elements for 3D printing applications.

2. Materials and mix design

2.1. Materials

Binder was composed of CEM III 42.5N (CEMEX, Germany) and limestone powder (Opterra, Germany) with specific gravities of 3.0 g/cm^3 and 2.7 g/cm^3, respectively. As aggregate, crushed basalt (Baden-Württemberg, Germany) with particle size up to 0.6 mm and

Table 1
Properties of basalt fibres (producer's data).

Material	Length [mm]	Thickness [μm]	Fracture strength [MPa]*	Thermostability at 200 °C (retained fracture strength) [%]	Thermostability at 400 °C (retained fracture strength) [%]	Water absorption
Basalt fibres	6	13 ± 1	2670 ± 5 %	95	82	Less than 0.1 %

* According to ISO EN 10618.

Table 2
Chemical composition of basalt fibres (producer's data).

Wt%	SiO_2	Al_2O_3	Fe_2O_3	CaO	MgO	TiO_2	Na_2O	Other
Min.	45	12	5	6	3	0.9	2.5	2
Max.	60	19	15	12	7	2	6	3.5

waste glass (WG) with specific gravities of 2.96 g/cm^3 of and 2.53 g/cm^3 were used, respectively. Brown soda-lime beverage glass was obtained from a local recycling company. Before use, it was washed, dried, milled, and sieved to 1 mm. Sika Control PerFin 300 (Sika Deutschland GmbH, Germany) defoaming admixture (density of 0.96 g/cm^3) and dispersed basalt fibres (density of 2.96 g/cm^3) with an average length of 6 mm produced by the Deutsche Basalt Faser GmbH (Germany) were used. Detailed information on the basalt fibres properties and chemical composition were summarised in Table 1 and Table 2, respectively.

To produce lightweight 3D printed composite, pre-wetted expanded thermoplastic microspheres (ETM) Expancel 461 WE 20d 36 (Nouryon AB, Sweden) with an apparent density of 36 ± 4 kg/m^3 were used. The particle size of the microspheres was equal to D50 of 20–30 μm (data provided by the supplier). The particle size distributions of used dry materials, determined via laser diffraction particle size analyser Mastersizer2000 (Malvern Panalytical Ltd., UK), are depicted in Fig. 1. The spherical morphology and narrow particle size distribution of ETM particles were confirmed by scanning electron microscope (SEM) analysis and are presented in Fig. 2. More detailed characterisation of as-received materials can be found in the previous study of Cuevas et al. [27].

2.2. Mixture design

Mixture compositions were developed through a series of initial trials with fixed cement content principles. Six 3D printable mixtures were initially developed and tested to choose the most suitable material for large-element printing. Three normal-weight mixtures without ETM presence with 0 %, 50 % and 100 % volume replacement levels of basalt aggregate with WG were designed and designated as G0, G50 and G100, respectively. The control mixture containing 100 % of basalt aggregate was designated as G0. Additionally, the second set of three lightweight mixtures with the addition of 3 wt% (by mass of binder) of ETM and the same replacement levels of aggregate were produced and designated with the same principle as normal-weight mixtures (G0-ETM, G50-ETM, G100-ETM).

The water-to-binder ratio (w/b) ranged between 0.35 and 0.39, and the aggregate-to-binder (a/b) was 0.44 in all samples. Slight modifications in the mixture composition of 3D printed materials were required to ensure proper printability of material and

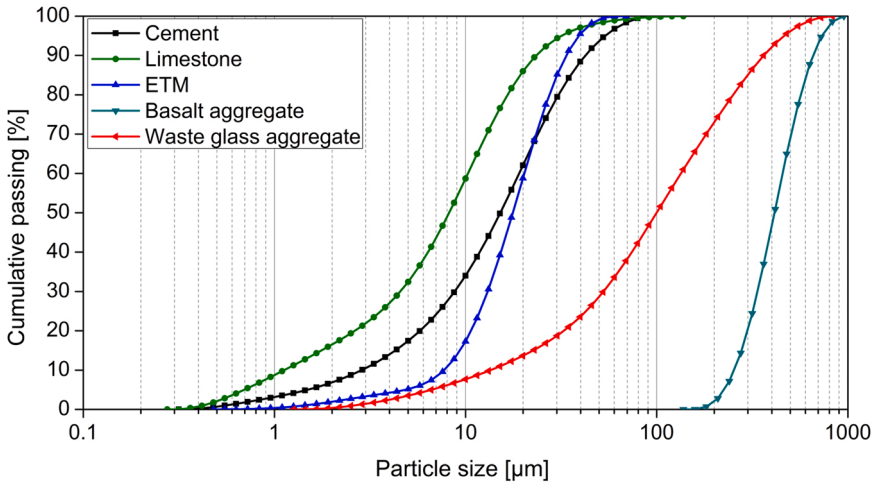

Fig. 1. Particle size distribution of cement, limestone, expanded thermoplastic microspheres, basalt and waste glass aggregates. Reprinted from Cuevas et al. [27].

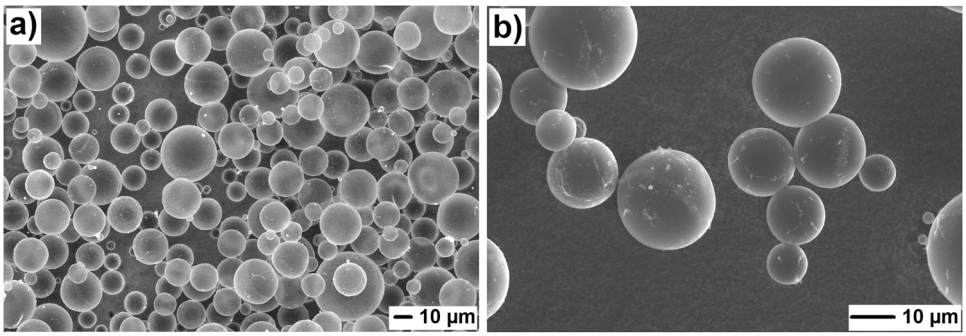

Fig. 2. SEM micrographs of expanded microspheres.
Reproduced from Cuevas et al. [27].

Table 3
Mass-related mixing ratio [27].

Mix designation	Binder	w/b	Expanded microspheres***	Basalt aggregate	Waste glass	PerFin 350 [%]***	Fibres [%]***
G0	1*	0.35	-	0.44	-	0.7	0.3
G50	1**	0.37	-	0.22	0.22	0.7	0.3
G100	1**	0.38	-	-	0.44	0.7	0.3
G0-ETM	1*	0.37	0.03	0.44	0.00	0.7	0.3
G50-ETM	1**	0.38	0.03	0.22	0.22	0.7	0.3
G100-ETM	1**	0.39	0.03	-	0.44	0.7	0.3

* Cement:limestone ratio 1:0.52.
** Cement:limestone ratio 1:0.49.
*** By weight of binder.

consistency with targeted flow between 135 and 165 mm (according to EN 1015-3). Therefore, due to the replacement of basalt aggregate with WG slight increment of water and decrement of limestone powder was required. This is attributed to higher finesses of WG as a result of the milling process, thus higher water absorption. Similarly, despite using pre-wetted ETM, a slight increment of water was also required to meet the consistency required for the mixture to be printed. The defoaming agent and fibre content were set constant to 0.7 % and 0.3 % by mass of binder, respectively. The mixture composition of 3D printable composites was summarised in Table 3, while the basic properties of the developed material were presented in Table 4. Detailed information on the fresh properties and printability characteristics of the mixtures above can be found in the author's previous study [27].

2.3. Wall printing process

Printable composites were mixed using a standard rotary mixer confirming to EN 196-1 with a mixing procedure as follows: (i) dry components mixing – 1 min, (ii) mixing with water and admixture at 140 rpm – 1 min, (iii) rest – 1 min, (iv) high-speed mixing (285 rpm) – 2 min. Afterwards, the mixture was transferred to the 3D printer. Large wall elements and testing specimens were printed using an XYZ-gantry system equipped with a TU Berlin-developed active pumping nozzle for filament deposition. The following printing parameters were used during the printing process:

- a nozzle diameter of 8 mm,
- a print path of 10 mm width and 4.5 mm height,
- an average volume flow of 1800 mm^3/s,
- printing speed 0–60 mm/s (according to 0–2700 mm^3/s).

Based on the thermal simulation, the most representative wall topology variant was chosen and a set of wall elements were printed. Three repetitive sections of wall element were selected to be printed using G0 and G50-ETM mixtures with the final element size of 30 (width) × 90 (length) × 45 (height) cm^3. The g-code model and final printed element are presented in Fig. 3.

3. Testing procedures

The experimental protocol of this research work is depicted in Fig. 4. The research framework was divided into three stages: (i) material characterisation, (ii) building envelope thermal simulation, and (iii) numerical simulation, wall element printing, and verification. In the first part of the work, small-scale specimens were tested to determine the basic fresh and hardened properties of the developed 3D printable composites. Afterwards, selected data were used as input parameters for the thermal simulation of building

Table 4
Comparison of the basic parameters of developed mixtures determined after 28 days of curing used for further evaluations from Cuevas et al. [27].

Mix designation	Oven-dry density [kg/m^3]	Thermal conductivity [W/m/K]	Compressive strength [MPa]	Flexural strength [MPa]
G0	1852 ± 15	0.74 ± 0.02	44.9 ± 3.1	8.0 ± 0.2
G50	1806 ± 20	0.66 ± 0.02	46.3 ± 1.4	8.2 ± 0.2
G100	1767 ± 16	0.62 ± 0.02	46.4 ± 2.7	8.7 ± 0.4
G0-ETM	1457 ± 13	0.47 ± 0.01	18.3 ± 2.1	4.8 ± 0.3
G50-ETM	1421 ± 12	0.46 ± 0.01	21.3 ± 2.1	4.5 ± 0.4
G100-ETM	1411 ± 10	0.45 ± 0.01	23.9 ± 1.5	5.0 ± 0.2

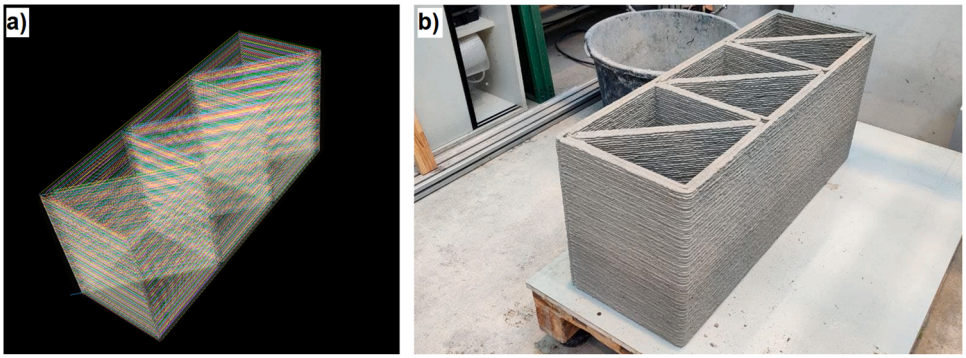

Fig. 3. G-code visualisation (a) of wall element and final 3D printed element (b).

envelopes. Based on the thermal simulation, an optimal wall topology variant was chosen and printed for mechanical testing (verification).

3.1. Thermal simulation studies

Simulation studies were aimed to find the most optimal wall topology that satisfies thermal insulating performance and has appropriate economic aspects, including the amount of printed materials (i.e., solid content in the envelope). Based on the data presented in the thermal simulation (see Section 4.1), G0 (normal-weight mixture), and lightweight mixture G50-ETM were selected. G0 was chosen as a representative (control) mixture, while G50-ETM was found to exhibit almost comparable thermal conductivity performance as G100-ETM with higher mechanical performance [27]. The selection of the final material used for thermal and numerical simulations will be comprehensively described in the result section (Section 4.1).

Heat transfer calculations for individual models of printed walls were executed employing THERM software (version 7.8),

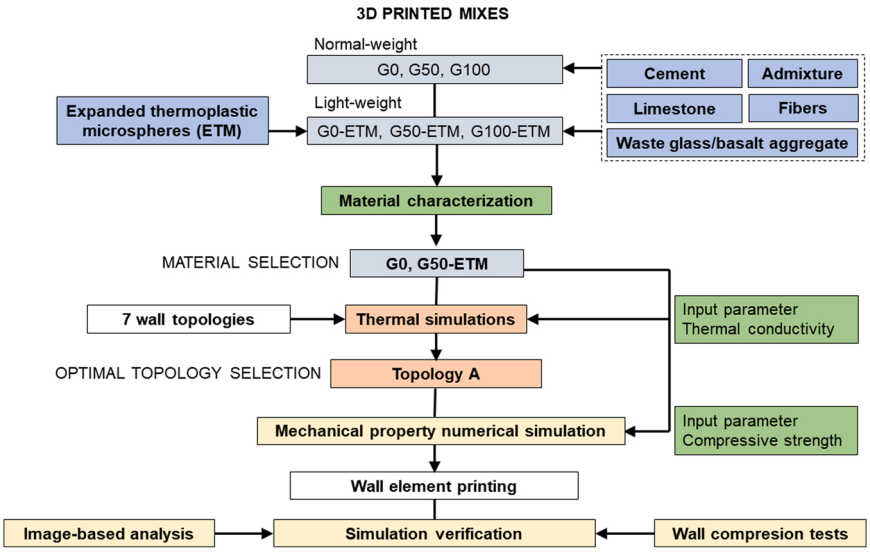

Fig. 4. Experimental framework for research.

developed at Lawrence Berkeley National Laboratories (LBNL) based on the finite element method. A flat, two-dimensional longwall model with a length of 2.0 m and a width of 0.30 m was adopted. The following boundary conditions were established: internal temperature $\theta_i = 20.0$ °C, external temperature $\theta_e = -16.0$ °C, internal film coefficient $\lambda_{si} = 7.69$ W/(m^2 K), external film coefficient $\lambda_{se} = 25.00$ W/(m^2 K). The edges of the section were modelled as adiabatic.

Seven variants of wall topology (Fig. 5) were proposed with similar wall widths of 30 cm, and the printed concrete path's thickness corresponded to the average printing path (2 cm). The simulations were made for the wall produced with mixtures G0 ($\lambda_{mix1} = 0.74$ W/(m K)) and G50-ETM ($\lambda_{mix6} = 0.45$ W/(m K)). In each variant, three potential types of filling of the printed wall were tested: stationary air, foam concrete ($\lambda_{cfoam} = 0.14$ W/(m K)) [28], and insulating polyurethane foam ($\lambda_{pfoam} = 0.030$ W/(m K)). The heat transfer coefficient, U, and the lowest temperature on the inner wall surface were determined for each model. The models meet the requirements of the EN ISO 10211 standard [29].

3.2. Mechanical property evaluation using simulation

The simulation is conducted using ABAQUS 2021 software, developed by ABAQUS Inc., to predict the failure behaviour of the wall structure before the actual experiment [30]. Because the compression test of the printed wall structure was conducted after 28 d, the hardened concrete behaviours were considered during the simulation. The simulation was performed in two steps: 1) with the elastic material and 2) considering failure behaviour. The first step was used to focus on the elastic behaviour of the wall structure before failure. The region where the stress is concentrated or where a failure might occur can be identified through the elastic analysis. After that, the failure behaviour of the wall element was evaluated using the concrete damage plasticity (CDP) model; it is usually used to describe the concrete damage evolution [31]. It is required to conduct the experiment to determine the input modelling parameters for the CDP model. However, the assumed values for the input modelling parameters are used here to simplify the problem because the simulation aims to show the plausibility of the proposed framework towards sustainable lightweight 3D printed wall building development. Nevertheless, all parameters are calibrated based on the experiment results at the material/element scale (Section 4.4).

To compare the behaviour of the wall according to the mix design, two different models were designed and printed using mixtures G0 and G50-ETM. Based on the author's previous research [27], the compression strength (f_c) and tensile strength (f_t) were taken as 44.9 and 8.0 MPa for G0, and 21.3 and 4.5 MPa for G50-ETM. The Young's modulus for each case was calculated from ACI 318 [32], the relationship between Young's modulus and compression strength, were selected as 22.3 and 10.8 GPa for G0 and G50-ETM, respectively. The Poisson's ratio (ν) was set to 0.2 in both cases. The density was selected from the measurement data. Table 5, sourced from the literature [33], provides the rest of the parameters considered for the simulation.

Based on the values for the CDP model, the material parameters are assigned for the elastic analysis. The interlayer bonding behaviour between layers is not considered, as all printed layers along the height direction are considered to have rigid link connections (similar to hardened concrete). Based on the nozzle width and the printing pattern, the inter-filament pore, located between the printed filament and mainly concentrated at the corner of the printing pattern, is a crucial factor in structural failure. The weakest region in the 3D printed structure might be the region with the greatest material loss. Therefore, the properties of inter-filament regions and their impact on structural integrity should be carefully considered.

3.3. Wall testing

As described in Section 2.3, three printed wall elements were tested in a displacement-controlled compression test. During the test, an optical stereo camera system was employed to measure deformations and surface strains of the printed wall elements (Fig. 6). The measurement method of the ARAMIS 4M sensors manufactured by GOM GmbH, Germany, is based on the principle of digital image correlation (DIC). The system operates contactless with two cameras for 3D measurements. The surface of the wall elements was prepared with a random black-and-white pattern to generate the grey value information to be evaluated in the camera images. The device can measure displacements and strains on the visible surface in any desired direction using just one sensor and two cameras. The strain calculation is based on the recorded displacement field of recognised image areas, so-called facets [34]. Chaves Figueiredo et al.

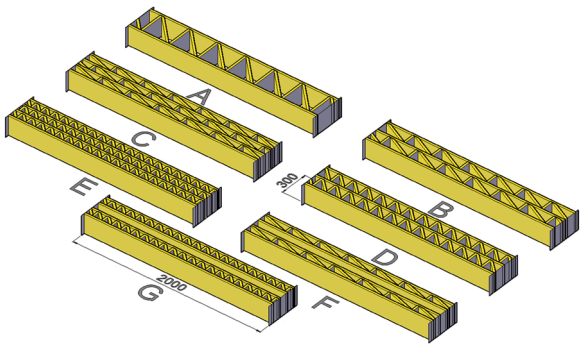

Fig. 5. Evaluated wall system topologies.

Table 5
Material properties of concrete damaged plasticity model. (Note that α is the dilation angle, Kc is the parameter related to yield surface, e is eccentricity, and fb_0/fc_0 is the ratio between the concrete strength for biaxial and uniaxial loading.).

α	Kc	e	fb_0/fc_0	Viscosity parameter
35	0.667	0.1	1.16	0.008

[35] applied a similar DIC method for specimens undergoing tensile testing.

4. Results and discussion

4.1. Material characterisation

Fig. 7 presents the thermal conductivity and mechanical properties of all developed mixtures after 28 d of curing. It can be seen that lightweight mixtures (G0-ETM, G50-ETM, G100-ETM) show substantially lower thermal conductivity than normal-weight mixtures (G0, G50, G100), due to considerably lower density resulting from the introduction of expanded thermoplastic microspheres. G50-ETM (0.46 W/m K) and G100-ETM (0.45 W/m K) exhibited slightly lower thermal conductivity values than G0-ETM (0.47 W/m K) as a result of waste glass presence in the mix. The inclusion of ETM and waste glass led to a substantial decrement in the oven-dry density of the material from 1852 kg/m^3 (G0) down to 1421 kg/m^3 and 1411 kg/m^3 for G50-ETM and G100-ETM, respectively. Compressive strength and flexural strength values are presented in Fig. 7**b**. Substantial differences between two normal-weight and lightweight concrete are visible due to density variation. Due to decreased material density, the mechanical performance of lightweight mixtures was also decreased. However, lightweight specimens still demonstrated compressive strength values between 18 and 24 MPa, making this mixture suitable as a load-bearing application.

Based on the obtained values for printed specimens regarding mechanical and thermal performance as well as results of flowability (fresh properties characterisation) [27], the lightweight 3D printable mix (G50-ETM) was chosen for further evaluation. For comparison purposes, the normal-weight G0 mix was chosen as the reference mix.

4.2. Thermal transmittance

The results of thermal transmittances (U-values) are presented in Fig. 8. Three groups of results can be distinguished, corresponding to the filler of the printed wall. In all variants, the wall structures made of G50-ETM achieved lower thermal transmittance values. However, the results indicated that the filler had a more significant influence on the U-value. Variants with no filling materials (i.e., air-filled) should be considered separately from the other two. In the case of air, the number of independent chambers greatly influenced the improvement of the U-value. The more closed spaces in the wall, the better the U-value result was obtained. Variant E turned out to be the best variant in this group. The effect has to be associated with the increased number of chambers in this variant, which subsequently increase the surface resistance to heat transfer between the air and the printed concrete path.

In the case of variants filled with foam concrete and polyurethane foam, the best variants turned out to be A, B and F. The presented results prove that considering the U-values, the tested printed walls are acceptable and can be used both in warm climates, where U-value should be less than 0.7 W/(m^2 K) (filling with foam concrete) and in cold climates, where the requirements for external walls are often below 0.20 W/(m^2 K) (filling with polyurethane foam). The problem with printed walls may be their heterogeneity. This characteristic may cause lower local temperatures on the inner surface of the wall, caused by the course of the printed pattern. Therefore, the analysed variants were tested under extreme conditions of external temperature of − 16 °C. Fig. 9 presents the results of this examination.

In the case of filling the walls with air, the temperature reduction on the inner surface was significant as expected. Such solutions are not suitable for such extreme conditions of the outside temperature. In the other two groups, the temperatures are relatively high.

Fig. 6. Wall element test setup with optical stereo camera system ARAMIS 4M.

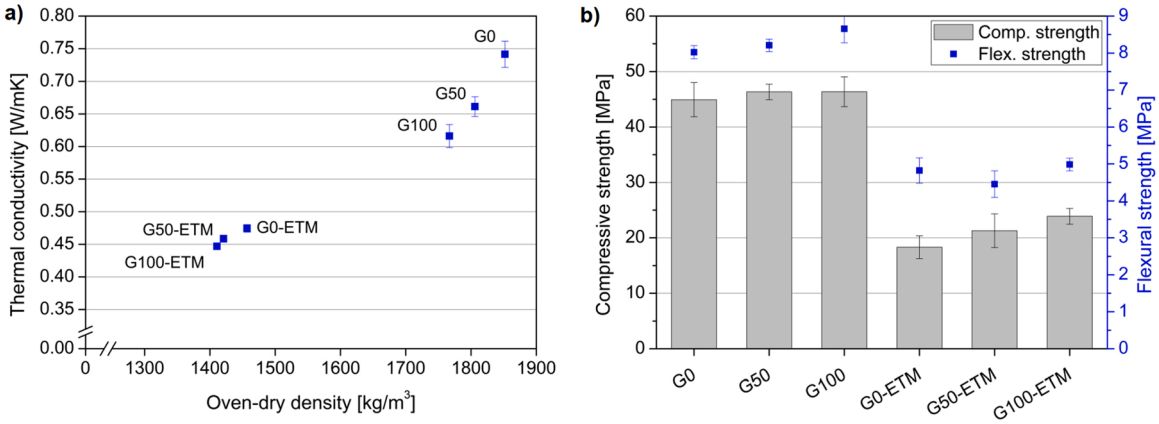

Fig. 7. Thermal conductivity of cast specimen as a function of oven-dry density (a) and mechanical properties of cast specimens after 28 d b). Based on Cuevas et al. [27].

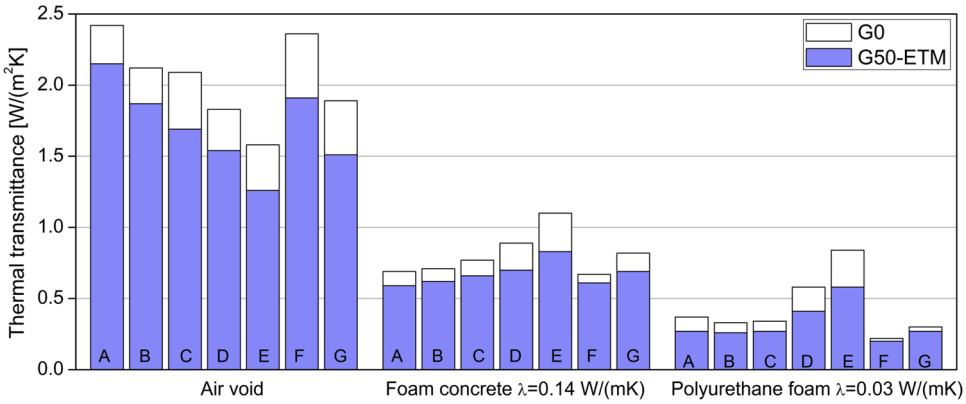

Fig. 8. Thermal transmittance of wall systems depending on the filler material.

The highest, and therefore the most favourable, were observed in C, F and G. In the F and G variants, there is a continuous layer of filling insulation, which stabilises the temperature on the inner side, thus reducing the variability of the inner surface temperature.

Based on internal temperatures, the temperature factors f_{Rsi} were calculated (Fig. 10). In the case of air filling, adverse values in the range of 0.67–0.84 were obtained. In walls filled with foam concrete filling, f_{Rsi} was 0.85–0.91, and in walls filled with polyurethane foam, 0.88–0.96. Thus, it can be assumed that the last two groups are protected against the local occurrence of surface condensation on the flat surface of the wall.

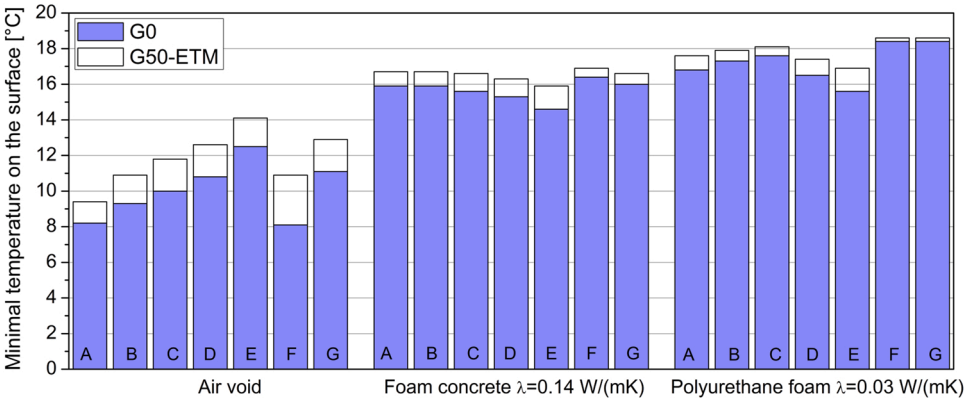

Fig. 9. Minimal temperature vs type of wall system and filler (note: opposite colours were assigned compared to Fig. 8).

The correlation between the *U*-value and the ratio of the printed path's area to the total section area of the tested walls is shown in Fig. 11. As evident, the thermal transmittance values are satisfactory even if the solid content of some systems has increased. Therefore, no clear association between the lowest amount of solid printed material and having the best performance has been identified. However, it can be observed globally that in the case of variants with foam concrete or polyurethane foam filling, the *U*-value increases with the increase of the solid content. This suggests F, C and B to be the most suitable for that purpose. In the case of variants with air, the increase in the number of closed chambers causes a reduction in heat transfer; thus, lower values were obtained with high solid content.

Fig. 12 shows the relationship between the minimal surface temperature and the quotient of the area of the printed path to the total section area of the tested walls. In the case of air filling, some correlation appears between the solid area and the surface temperature. The higher the solid content area, the higher temperatures were observed on the internal surface of the tested variants. However, the correlation is insignificant in the other two groups filled with foam concrete and polyurethane foam. This could mean that the shape of the printed path of the concrete itself is more important than its overall content.

As in the case of surface temperatures, a certain trend was observed between the temperature factor f_{Rsi} and solid content (Fig. 13) in variants with air voids. With the increase in solid content (and also an increase in the number of closed chambers), the temperature factor was clearly greater. In the case of filling with foam concrete or polyurethane foam, there is a slight descending trend.

Table 6 presents a summary of the printing efficiency of each variant. The variants that require less material are better, in terms of speed and difficulty, at printing a given shape. Variants containing a lower *U*-value are considered more optimal. Therefore, both *U* and *A* are included in the denominator. With these assumptions, the A and F variants are the most efficient in both filling groups.

Fig. 14 presents the results of simulation variants of printed walls without infill material (hollow walls). Attention should be paid to completely different scales of heat flux density and temperature when compared to walls containing infill material (Fig. 15 and Fig. 16). The obtained results confirm much higher values of heat flux of these variants, which simultaneously resulted in a significant temperature reduction within the entire cross-section of individual variants compared to walls with infill. The lowest and, at the same time, the most homogeneous heat flux values within the entire cross-section were observed in variants E and G. As a consequence, it made it possible to obtain relatively homogeneous temperature distributions in these variants compared to the others. The cross-sections obtained from the simulation confirm that in the case of hollow walls (without infill), a major factor governing the thermal performance is the number of closed chambers. The greater the number, the lower the heat transfer values were obtained. This is due to the occurrence of additional surface thermal resistances that occur at the contact point between the printed path and the air in a given chamber. However, as presented in this section the major factor governing the thermal performance of printed envelopes is the infill material.

In Fig. 15, the flux magnitudes of each variant with infill material are shown. The differences between the foam concrete and polyurethane foam variants are visible. In the variant with the foam concrete, the flux magnitudes values in the filler are much higher than in the polyurethane foam filler. At the same time, in the variants with the foam concrete, the printing path is described with higher flux density values than in the PF variant. The use of a printed path perpendicular to the wall surface seems to be very unfavourable due to the high values of heat flux. The paths made at the smallest possible angle to the wall surface are characterised by much lower heat flux values. The continuous filling in the central part of the wall cross-section (variants F and G) enables to obtain an insulating layer with very low and homogeneous heat flux values.

Fig. 16 shows the temperature distribution in individual variants. The diagrams of variants filled with polyurethane foam are characterised by slightly higher differences in temperature distribution. The highest discrepancies can be observed in variants F and G. In this case, polyurethane foam as a continuous layer in the middle causes a significant unification of the temperature gradient.

Based on the data available from this section, topology A has been chosen for further investigations. Despite slightly less efficient thermal performance than other topologies (C, E, F), topology A possesses the lowest solid content (printing area). Thus substantial savings on printing can be achieved (see Table 6). In this case, the values of minimal internal surface temperatures and temperature factors are also acceptable and comparable to other variants. Moreover, in standard practice, utilisation of polyurethane foam as an

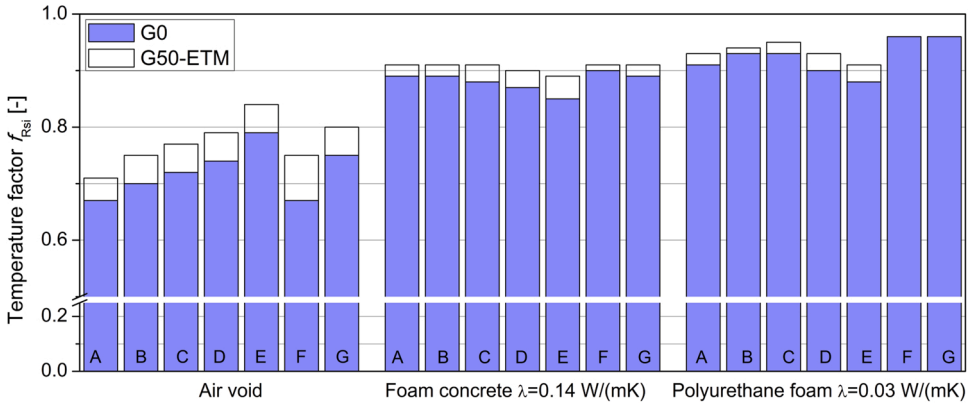

Fig. 10. Temperature factor f_{Rsi} vs type of wall system and filler (note: opposite colours were assigned compared to previous Fig. 8).

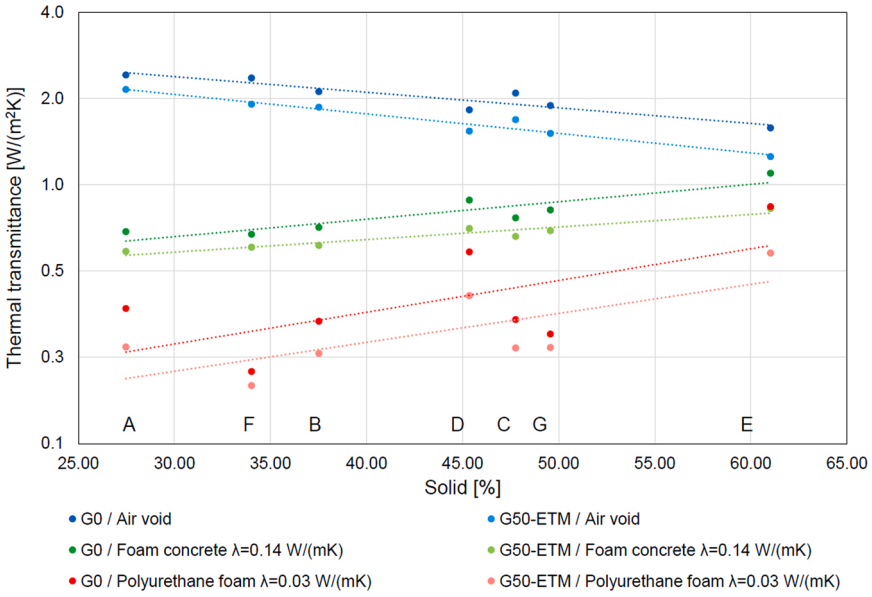

Fig. 11. *U*-value as a function of the solid content of each printed wall system.

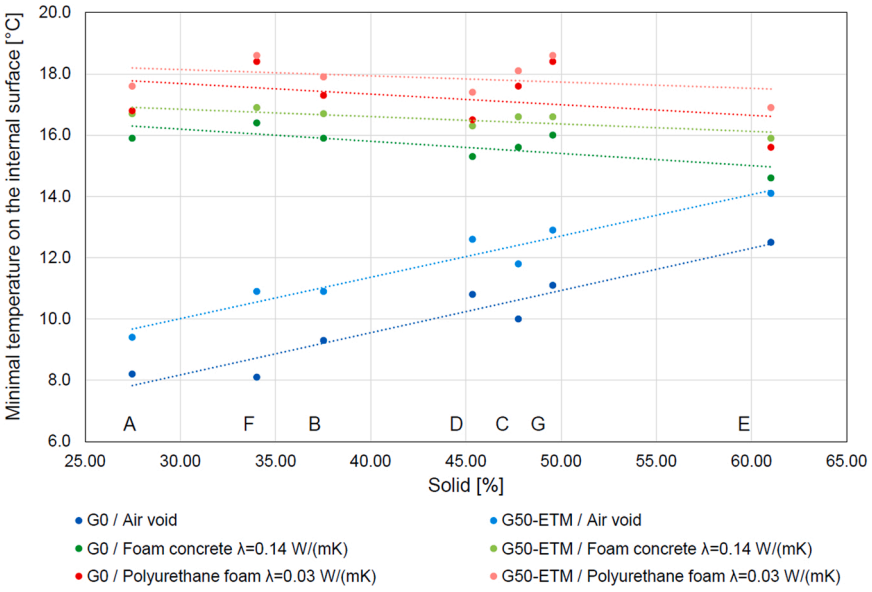

Fig. 12. Minimal temperature as a function of the solid content of each printed wall system.

insulating material is not encouraged due to its discursive environmental impact. Therefore, foam concrete could be an economical and environmentally viable solution.

4.3. Theoretical load capacity

Load capacity analysis results are shown in Fig. 17. The von Mises stress distributions are plotted, and each result is obtained at the same load step. Notably, the simulation of Variant A was also conducted, but the result will be discussed later in this section. In most cases, it is found that the cracks begin around the connection area between the inner and outer walls, and cracks in the middle wall are propagated successively, as shown in Fig. 17. Variants B and F have larger displacement along horizontal direction than Variants D, E, and G, resulting from larger spans (interval) of inner walls. For additive manufacturing, the debonding properties of the surface where the printed layers meet are one of the dominant factors in determining the performance of the 3DCP structure. To prevent the debonding between inner and outer walls or detachment of the outer wall printing layers, shorter distances (intervals) between inner

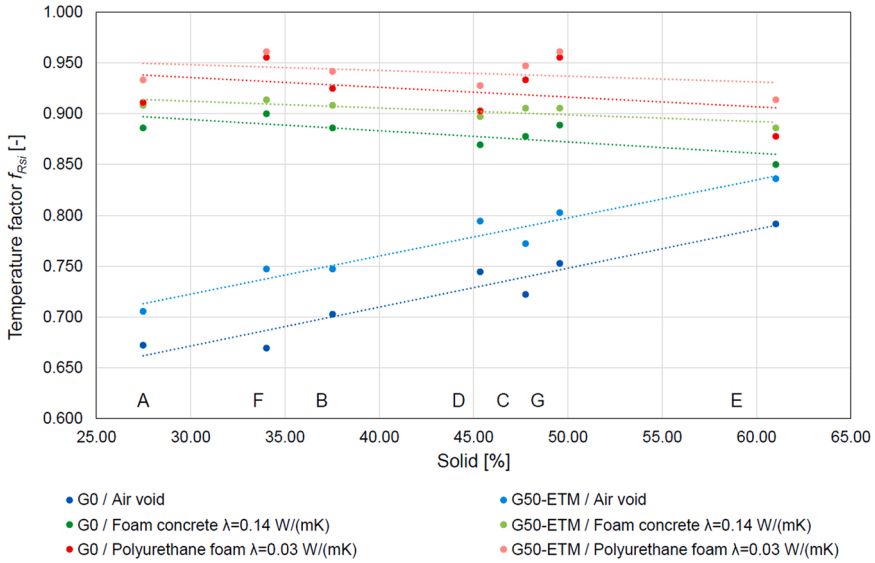

Fig. 13. Temperature factor as a function of solid content of each printed wall system.

Table 6
Efficiency of using particular topologies.

Variant	Solid – *A* [%]	*U*-value foam concrete [W/m^2 K]	Topology efficiency 1/ (*AU*) [%]	*U*-value polyurethane foam [W/m^2 K]	Topology efficiency 1/ (*AU*) [%]
A	27.5	0.586	6.21	0.272	13.39
B	37.5	0.615	4.33	0.258	10.33
C	47.8	0.661	3.17	0.270	7.76
D	45.4	0.705	3.13	0.411	5.37
E	61.0	0.828	1.98	0.578	2.83
F	34.0	0.606	4.85	0.199	14.75
G	49.6	0.692	2.91	0.271	7.45

walls can be implemented. When comparing the load-bearing capacities of all patterns, including Pattern A, the stress distributions and crack patterns are similar to each other. Therefore, Variant A is selected as a representative model for a better understanding of the behaviour of wall elements by combining experiments (mechanical testing and DIC analysis), where the behaviour between the inner and outer walls can be most clearly and accurately investigated.

Table 7 presents the load-bearing capacity analysis results, where all wall variants were simulated using mixture G0. Additionally, variant A using G50-ETM is included for comparison in Section 4.4 between simulation results and experimental results obtained from the compressive strength test. In Table 5, the peak stress corresponds to the load-bearing capacity of the wall for the cross-section area of each topology. Variants A and E show the lowest and highest load-bearing capacity and peak stress, respectively. Despite variant A having the lowest load-bearing capacity of all wall topologies, it can still be used as a load-bearing element. Variant A has the lowest cross-section area; thus, it has the lowest solid content. Therefore, this topology is the most economically viable option.

4.4. Comparison of experimental and simulation results

To predict the failure behaviour of the wall structure before the printed wall experiment, the simulation was conducted using variant A with two different mixtures (i.e., G0 and G50-ETM). The mechanical results of the elastic analysis for G0 are shown in the upper row in Fig. 18. As shown in Fig. 18, the von Mises stress is maximised near the boundary of the inner and outer walls. At the top view, it seems that the outer wall experiences buckling-shaped behaviour, which is deformed in the direction perpendicular to the wall surface. When the printed layers and filaments consisting of the 3D printed wall element are well bonded to each other so that the structure behaves like the cast one, the structure can resist the stress on the inner/outer wall boundary and the perpendicular deformation on the outer wall. However, in the actual case, the printed wall has empty areas without material, especially near the connecting points (e.g., corner, border of the inner and outer wall); it is because the extruded material could not fill the entire area of the print path during printing when changing the direction of path (nozzle). Therefore, it can be expected that the failure of the structure could be started near the connections between the inner and outer walls.

From the failure analysis using CDP model, the displacement contours in the *y*-direction and damage index contours for G0 and

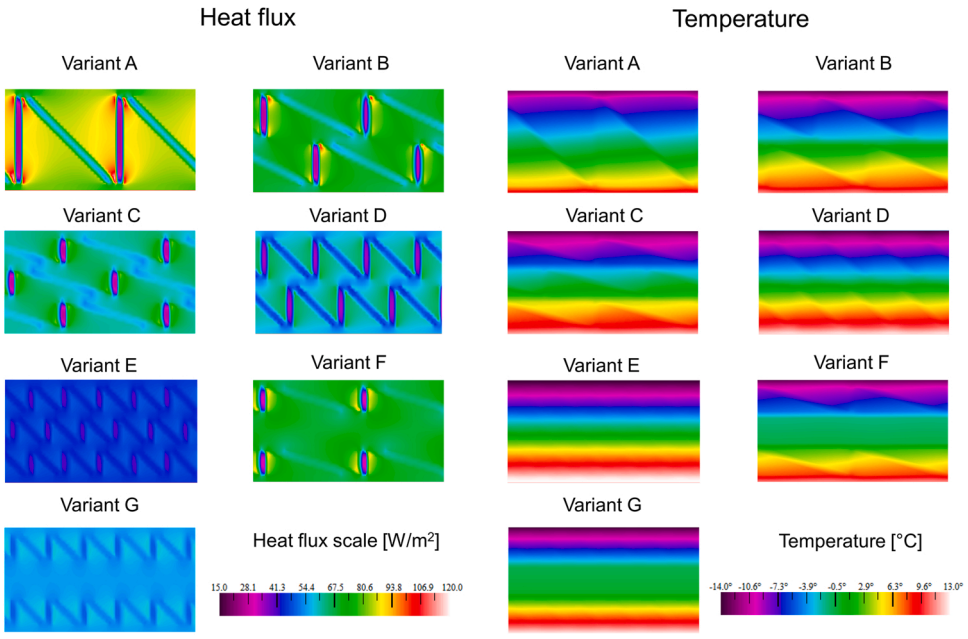

Fig. 14. Heat flux magnitude (left) and top view of the temperature distribution (right) of hollow walls (without infill material) with different topologies.

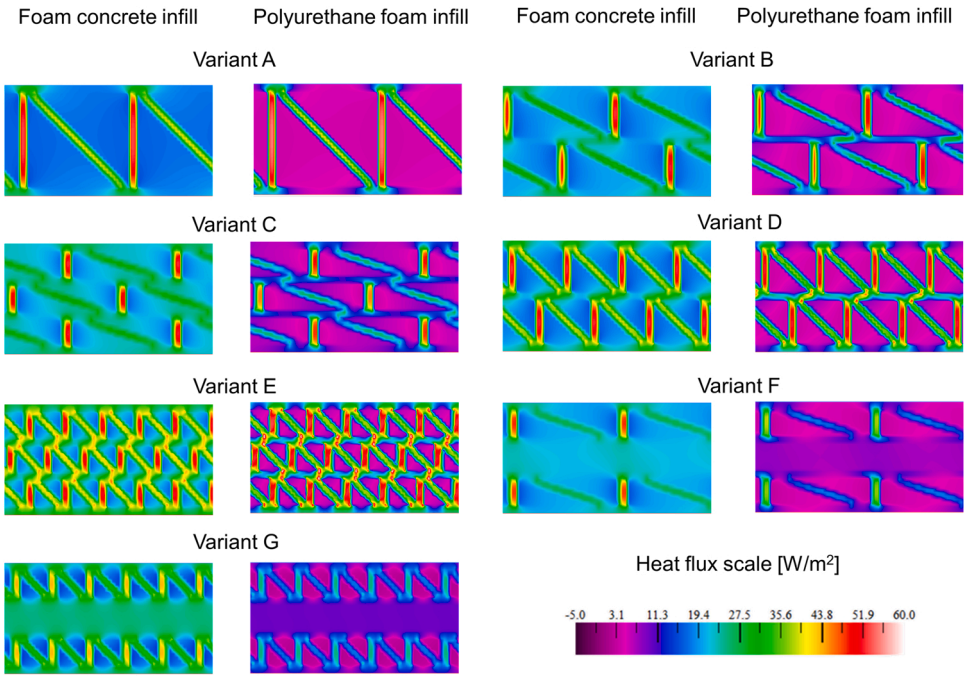

Fig. 15. Heat flux magnitude of walls with different topologies depending on the type of infill material (note: different heat flux scale when compared to Fig. 14).

G50-ETM at the same strain level are shown in the middle and the bottom of Fig. 18. The outer wall in the middle section (red circle in Fig. 18) has large perpendicular (*y*-dir.) deformation, leading to damage in the tensile direction in both mixtures. Especially in G0, there is no compression damage, while G50-ETM experiences severe concrete compression damage due to its weaker mechanical properties than G0. In either case, the cracks do not predominantly follow the connection region between inner- and outer-walls, rather occur through the outer or inner wall itself. From the results, it can be said that if there is any defect or weak connecting points in the 3D printed structure, cracks or damages can occur in the centre of the wall regardless of where the inner wall is connected and follow

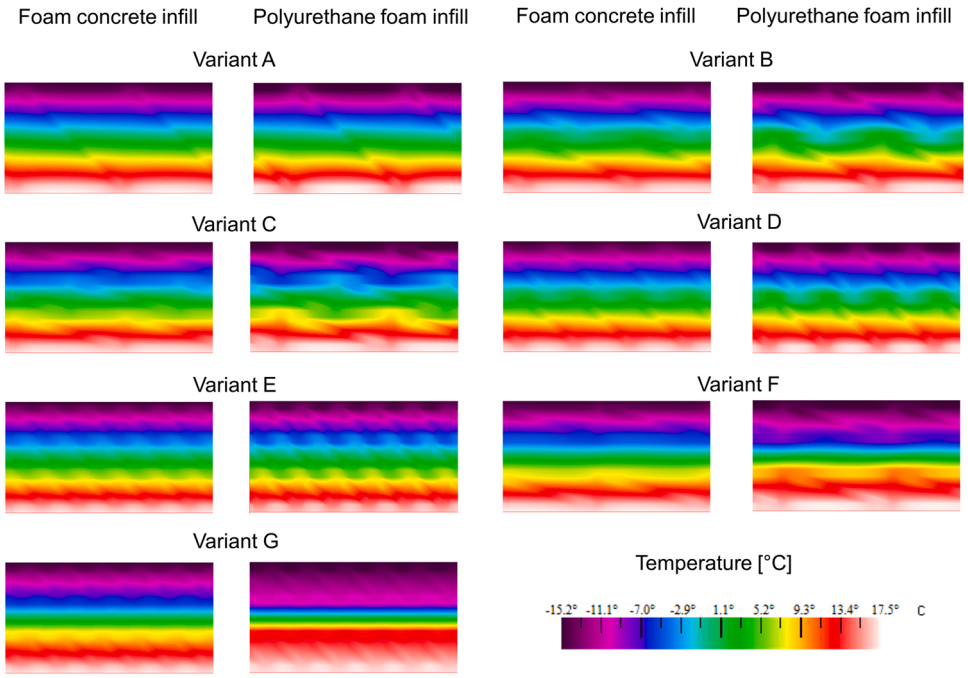

Fig. 16. Top view of the temperature distribution of walls with different topologies depending on the type of infill material (note: different temperature scale when compared to Fig. 14).

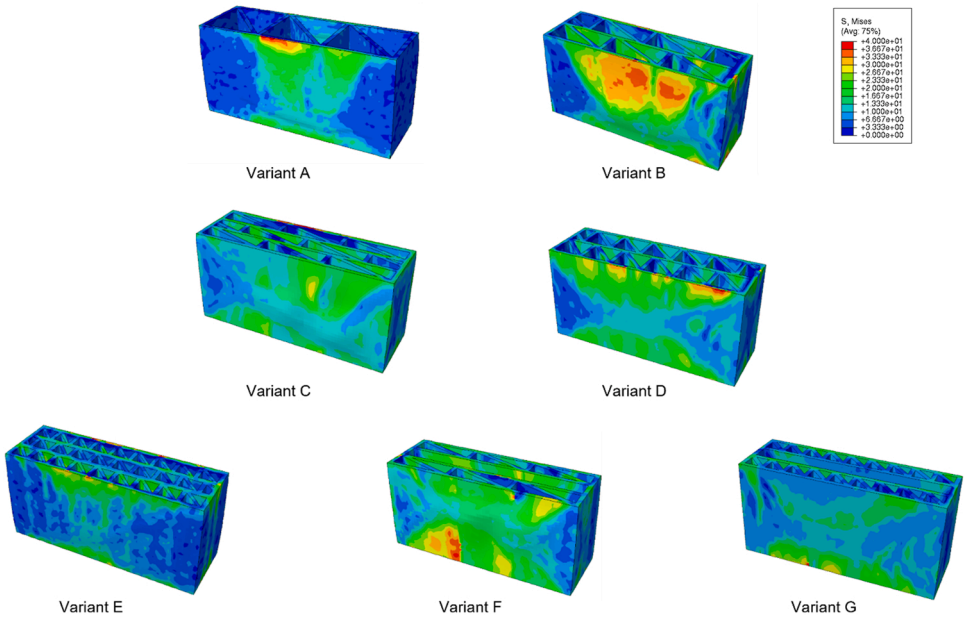

Fig. 17. Load capacity analysis results for all patterns with mix G0.

the tension failure behaviour. It should be noted that the bonding property between inner-outer walls, inter-filament and layer, needs to be considered when the purpose of the simulation is the precise analysis of the printed structural behaviour. However, due to the scope of this work, the simulation was conducted by simplifying the model with the assumption of a fully connected condition for every filament and layer.

To compare the simulation results with the experiment, the digital image correlation (DIC) analysis was conducted, as described in Section 3.3. Six 3D-printed wall elements with variant A were tested under compressional load; three were produced with G0 and the other with G50 ETM (see Fig. 19). As the results from the simulation show slight variation between the two mixtures, the DIC analysis

Table 7
Load-bearing capacity analysis results.

Variant	Mixture	Peak stress (MPa)	Cross-section area (mm^2)	Load bearing capacity (kN)
A	G0	39.0	84,189	3283
A	G50-ETM	19.5	84,189	1641
B	G0	39.3	121,063	4755
C	G0	45.3	135,260	6125
D	G0	44.6	128,832	5747
E	G0	45.7	170,703	7795
F	G0	44.5	114,484	5094
G	G0	44.5	138,139	6151

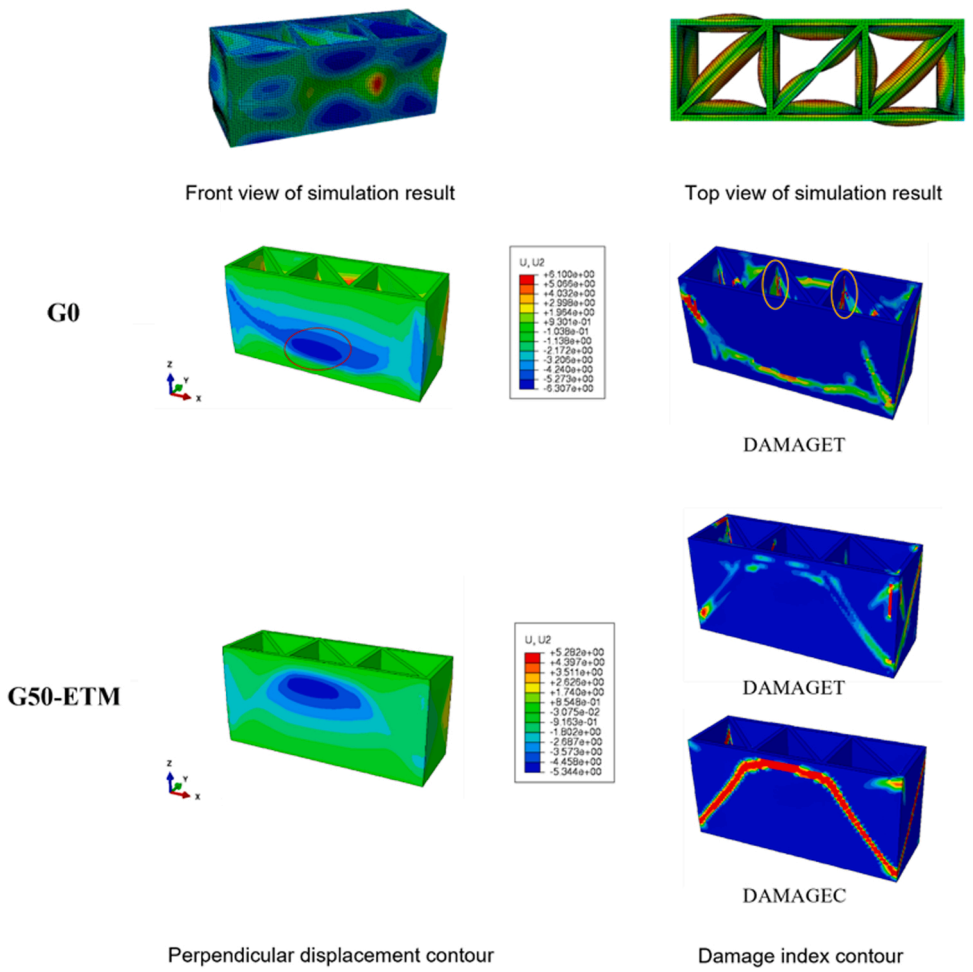

Fig. 18. Simulation results: (upper) elastic analysis results, (middle) failure analysis results of G0 and (bottom) G50-ETM using CDP model.

was performed only on the mixture G50-ETM.

Using the cross-section value for variant A of 84,189 mm^2 from Table 7, the peak stress for the tested elements was calculated through the load-bearing values obtained directly from the compression test of the 3D printed wall. G0 wall elements had a peak stress of 21.97 MPa, 23.28 MPa and 24.35 MPa. G50-ETM elements had a peak stress of 17.16 MPa, 16.12 MPa and 16.64 MPa. The elements with the maximum and minimum peak stress values with G50-ETM are analysed using the ARAMIS system.

The displacement and strain measurements of the ARAMIS system show the crack development of the first and second wall elements of G50-ETM with increasing loading on the outer surface of the wall elements. Due to geometrical limitations, it was only possible to depict a part of the long side of the wall elements. Fig. 20 shows the horizontal strain distribution right before and after the compression failure of the first wall element. The maximum horizontal strain was detected along the vertical connection between the inner and outer walls. The first cracks appeared in that region. The cracks are mainly focused on the connection region due to the weak bonding between the inner and outer walls produced by the lack of material. Interestingly, the interlayer bonding does not affect the

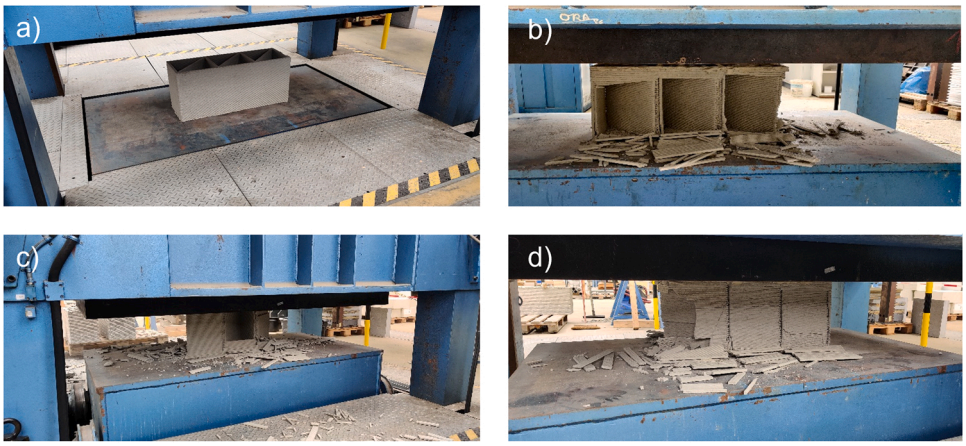

Fig. 19. G0 3D printed wall before testing (a), G0 3D printed wall after compressive strength test (b–d).

failure behaviour under the compression, which indicates the printed wall behaves with strong bonding between the layers in the lamination direction (horizontal); for future analysis using simulation, the bonding effect between the layers can be neglected, while the inter-filament bonding should be considered.

In addition, similarities in the displacement perpendicular to the wall surface can be observed between the numeric model and the measured data from testing the first and second wall elements of G50-ETM. As shown in Fig. 21, the deformation towards the inside and outside of the outer wall is observed from the simulation. In the DIC analysis, presented in Fig. 21, the displacement perpendicular to the wall surface right before compression failure with a buckling shape can also be seen in the numerical model (wall element 1: buckling shape in the middle zone, wall element 2: buckling shape in the left zone). The outer wall first resists the perpendicular deformation, then collapses or detaches from the wall after cracks appear and are propagated due to compression failure. For the second wall element, the evaluation of the horizontal and vertical strain distribution fits the failure point in the left zone, where the horizontal and vertical cracks meet (see Fig. 22). When the geometrical imperfection occurs during the printing process in the horizontal cracked region in Fig. 22, the inter-layer bonding is no longer assumed as an intimate bonding. It is necessary to consider the imperfection of the geometry during the simulation for a better understanding of the structural mechanical response.

5. Conclusions

A lightweight printable mixture was successfully developed and applied for the 3D printing of wall elements with optimal load-bearing characteristics. An additional normal-weight mixture was printed as a control specimen. Both mixtures proved to be printable and buildable for a final element size of 30 (width) × 90 (length) × 45 (height) cm^3.

The wall topologies studied in this work have the potential to use various infill materials to control the *U*-value, optimising the building envelope. There is no direct trend between solid content and thermal conductivity. Thus 3D printing opens many possibilities for designing the most optimal wall elements. For the selected topology, Variant A, mechanical simulations have shown that connections between inner and outer walls could start the collapse of the structure, independently of the mixture composition, as the results from the simulation show little variation between both mixtures studied.

The results from the DIC analysis identified the inter-filament weakness and the imperfections of the geometry of the printed

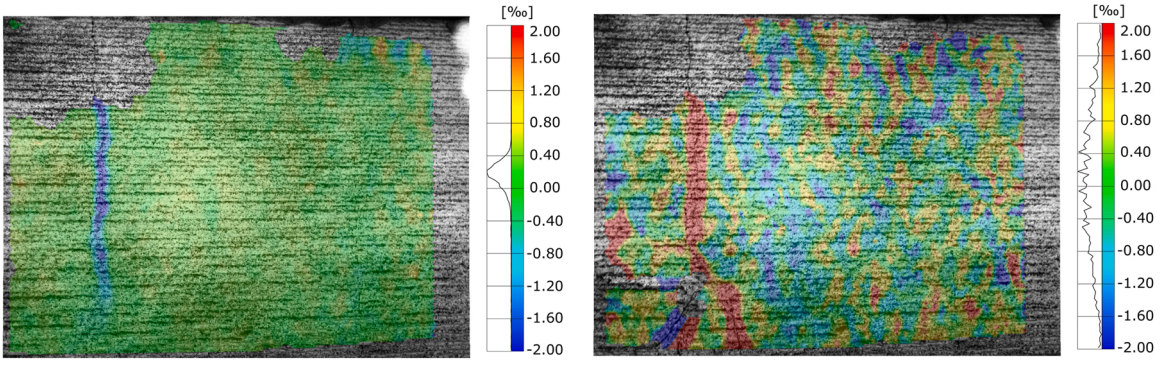

Fig. 20. Horizontal strain distribution [‰] obtained by optical measurement system ARAMIS of first wall element right before (left) and after (right) compression failure.

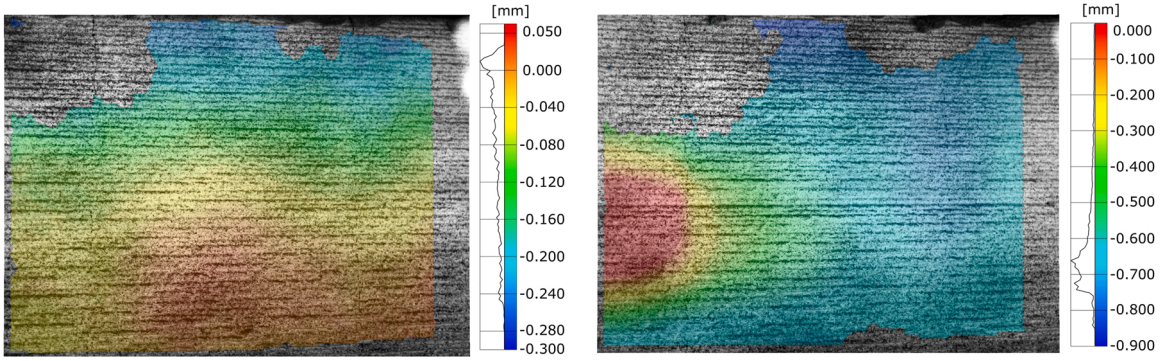

Fig. 21. Displacement perpendicular to the wall surface [mm] obtained by optical measurement system ARAMIS of first wall element (left) and second wall element (right) right before compression failure.

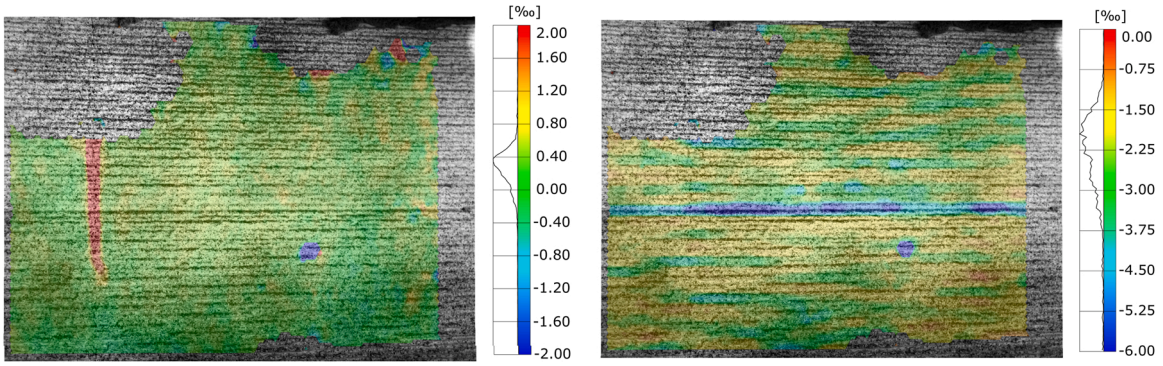

Fig. 22. Horizontal (left) and vertical (right) strain distribution [‰] obtained by optical measurement system ARAMIS of second wall element right before compression failure.

specimen as the main cause for failure, while the interlayer bonding itself proved not to substantially affect the structure under compression. Therefore, for future projects, the bonding between the internal and external layers should be improved and more realistic models should be developed to predict the collapse.

CRediT authorship contribution statement

Karla Cuevas: Conceptualization, Methodology, Investigation, Validation, Visualization, Formal analysis, Data curation, Writing – original draft, Writing – review & editing. **Jarosław Strzałkowski:** Methodology, Investigation, Validation, Data curation, Visualization, Writing – original draft, Writing – review & editing. **Ji-Su Kim:** Methodology, Investigation, Validation, Data curation, Visualization, Writing – original draft. **Clemens Ehm:** Resources, Methodology. **Theresa Glotz:** Methodology, Investigation, Validation, Visualization, Writing – original draft. **Mehdi Chougan:** Methodology, Validation, Writing – review & editing. **Seyed Hamidreza Ghaffar:** Methodology, Validation, Writing – review & editing. **Dietmar Stephan:** Methodology, Resources, Writing – review & editing, Funding acquisition, Supervision. **Pawel Sikora:** Conceptualization, Methodology, Validation, Visualization, Formal analysis, Data curation, Writing – original draft, Writing – review & editing, Project administration, Funding acquisition, Supervision.

Funding

This project received funding from the European Union's Horizon 2020 research and innovation program as part of Marie Skłodowska-Curie Grant agreement no. 841592. Additionally, this work was also supported by the Deutscher Akademischer Austauschdienst under Grant no. 57552340.

Declaration of Competing Interest

The authors declare that they have no known competing financial interests or personal relationships that could have appeared to influence the work reported in this paper.

Data Availability

Data will be made available on request.

Acknowledgements

We would like to thank Falk Martin from TU Berlin for support during printing and laboratory testing process. We acknowledge support by the German Research Foundation and the Open Access Publication Fund of TU Berlin.

References

[1] L. Reiter, T. Wangler, N. Roussel, R.J. Flatt, The role of early age structural build-up in digital fabrication with concrete, Cem. Concr. Res. 112 (2018) 86–95, https://doi.org/10.1016/j.cemconres.2018.05.011.
[2] P. Sikora, M. Chougan, K. Cuevas, M. Liebscher, V. Mechtcherine, S.H. Ghaffar, M. Liard, D. Lootens, P. Krivenko, M. Sanytsky, D. Stephan, The effects of nano- and micro-sized additives on 3D printable cementitious and alkali-activated composites: a review, Appl. Nanosci. 12 (2022) 805–823, https://doi.org/10.1007/s13204-021-01738-2.
[3] J. Xiao, S. Zou, Y. Yu, Y. Wang, T. Ding, Y. Zhu, J. Yu, S. Li, Z. Duan, Y. Wu, L. Li, 3D recycled mortar printing: system development, process design, material properties and on-site printing, J. Build. Eng. 32 (2020), 101779, https://doi.org/10.1016/j.jobe.2020.101779.
[4] T. Ding, J. Xiao, F. Qin, Z. Duan, Mechanical behavior of 3D printed mortar with recycled sand at early ages, Constr. Build. Mater. 248 (2020), 118654, https://doi.org/10.1016/j.conbuildmat.2020.118654.
[5] G. de Schutter, K. Lesage, V. Mechtcherine, V.N. Nerella, G. Habert, I. Agusti-Juan, Vision of 3D printing with concrete — technical, economic and environmental potentials, Cem. Concr. Res. 112 (2018) 25–36, https://doi.org/10.1016/j.cemconres.2018.06.001.
[6] Y. He, Y. Zhang, C. Zhang, H. Zhou, Energy-saving potential of 3D printed concrete building with integrated living wall, Energy Build. 222 (2020), 110110, https://doi.org/10.1016/j.enbuild.2020.110110.
[7] Z. Lu, B. Xu, J. Zhang, Y. Zhu, G. Sun, Z. Li, Preparation and characterization of expanded perlite/paraffin composite as form-stable phase change material, Sol. Energy 108 (2014) 460–466, https://doi.org/10.1016/j.solener.2014.08.008.
[8] A. Lotfy, K.M.A. Hossain, M. Lachemi, Lightweight self-consolidating concrete with expanded shale aggregates: modelling and optimization, Int. J. Concr. Struct. Mater. 9 (2015) 185–206, https://doi.org/10.1007/s40069-015-0096-5.
[9] A.L. Brooks, H. Zhou, D. Hanna, Comparative study of the mechanical and thermal properties of lightweight cementitious composites, Constr. Build. Mater. 159 (2018) 316–328, https://doi.org/10.1016/j.conbuildmat.2017.10.102.
[10] P. Pongsopha, P. Sukontasukkul, H. Zhang, S. Limkatanyu, Thermal and acoustic properties of sustainable structural lightweight aggregate rubberized concrete, Results Eng. 13 (2022), 100333, https://doi.org/10.1016/j.rineng.2022.100333.
[11] J. Strzałkowski, P. Sikora, S.-Y. Chung, M. Abd Elrahman, Thermal performance of building envelopes with structural layers of the same density: lightweight aggregate concrete versus foamed concrete, Build. Environ. 196 (2021), 107799, https://doi.org/10.1016/j.buildenv.2021.107799.
[12] J. Xiao, L. Hao, W. Cao, T. Ye, Influence of recycled powder derived from waste concrete on mechanical and thermal properties of foam concrete, J. Build. Eng. 61 (2022), 105203, https://doi.org/10.1016/j.jobe.2022.105203.
[13] M. Robati, T.J. McCarthy, G. Kokogiannakis, Incorporating environmental evaluation and thermal properties of concrete mix designs, Constr. Build. Mater. 128 (2016) 422–435, https://doi.org/10.1016/j.conbuildmat.2016.10.092.
[14] G. Ma, R. A, P. Xie, Z. Pan, L. Wang, J.C. Hower, 3D-printable aerogel-incorporated concrete: anisotropy influence on physical, mechanical, and thermal insulation properties, Constr. Build. Mater. 323 (2022), 126551, https://doi.org/10.1016/j.conbuildmat.2022.126551.
[15] L. Hao, J. Xiao, J. Sun, B. Xia, W. Cao, Thermal conductivity of 3D printed concrete with recycled fine aggregate composite phase change materials, J. Clean. Prod. 364 (2022), 132598, https://doi.org/10.1016/j.jclepro.2022.132598.
[16] L. Prasittisopin, K. Pongpaisanseree, P. Jiramarootapong, C. Snguanyat, Thermal and sound insulation of large-scale 3D extrusion printing wall panel, in: F. P. Bos, S.S. Lucas, R.J.M. Wolfs, T.A.M. Salet (Eds.), Second RILEM International Conference on Concrete and Digital Fabrication, Springer International Publishing, Cham, 2020, pp. 1174–1182.
[17] K. Dhasindrakrishna, K. Pasupathy, S. Ramakrishnan, J. Sanjayan, Effect of yield stress development on the foam-stability of aerated geopolymer concrete, Cem. Concr. Res. 138 (2020), 106233, https://doi.org/10.1016/j.cemconres.2020.106233.
[18] U. Berardi, C. Sprengard, An overview of and introduction to current researches on super insulating materials for high-performance buildings, Energy Build. 214 (2020), 109890, https://doi.org/10.1016/j.enbuild.2020.109890.
[19] D. Weger, H. Kim, D. Talke, K. Henke, T. Kränkel, C. Gehlen, Lightweight concrete 3D printing by selective cement activation – investigation of thermal conductivity, strength and water distribution, in: F.P. Bos, S.S. Lucas, R.J.M. Wolfs, T.A.M. Salet (Eds.), Second RILEM International Conference on Concrete and Digital Fabrication, Springer International Publishing, Cham, 2020, pp. 162–171.
[20] L. Wang, H. Jiang, Z. Li, G. Ma, Mechanical behaviors of 3D printed lightweight concrete structure with hollow section, Arch. Civ. Mech. Eng. 20 (2020), https://doi.org/10.1007/s43452-020-00017-1.
[21] M. Mohammad, E. Masad, S.G. Al-Ghamdi, 3D concrete printing sustainability: a comparative life cycle assessment of four construction method scenarios, Buildings 10 (2020) 245, https://doi.org/10.3390/buildings10120245.
[22] D. Lowke, E. Dini, A. Perrot, D. Weger, C. Gehlen, B. Dillenburger, Particle-bed 3D printing in concrete construction – possibilities and challenges, Cem. Concr. Res. 112 (2018) 50–65, https://doi.org/10.1016/j.cemconres.2018.05.018.
[23] R.A. Buswell, R.C. Soar, A.G.F. Gibb, A. Thorpe, Freeform construction: mega-scale rapid manufacturing for construction, Autom. Constr. 16 (2007) 224–231, https://doi.org/10.1016/j.autcon.2006.05.002.
[24] H. Marais, H. Christen, S. Cho, W. de Villiers, G. van Zijl, Computational assessment of thermal performance of 3D printed concrete wall structures with cavities, J. Build. Eng. 41 (2021), 102431, https://doi.org/10.1016/j.jobe.2021.102431.
[25] S.-Y. Chung, M. Abd Elrahman, P. Sikora, T. Rucinska, E. Horszczaruk, D. Stephan, Evaluation of the effects of crushed and expanded waste glass aggregates on the material properties of lightweight concrete using image-based approaches, Materials 10 (2017), https://doi.org/10.3390/ma10121354.
[26] A.V. Rahul, M. Santhanam, Evaluating the printability of concretes containing lightweight coarse aggregates, Cem. Concr. Compos. 109 (2020), 103570, https://doi.org/10.1016/j.cemconcomp.2020.103570.
[27] K. Cuevas, M. Chougan, F. Martin, S.H. Ghaffar, D. Stephan, P. Sikora, 3D printable lightweight cementitious composites with incorporated waste glass aggregates and expanded microspheres – rheological, thermal and mechanical properties, J. Build. Eng. 44 (2021), 102718, https://doi.org/10.1016/j.jobe.2021.102718.
[28] M. Abd Elrahman, P. Sikora, S.-Y. Chung, D. Stephan, The performance of ultra-lightweight foamed concrete incorporating nanosilica, Arch. Civ. Mech. Eng. 21 (2021), https://doi.org/10.1007/s43452-021-00234-2.
[29] EN ISO 10211:2017 – Thermal bridges in building construction — Heat flows and surface temperatures — Detailed calculations.
[30] D. Systemes, Abaqus 6.14—Abaqus Analysis User's Guide, Dassault Systemes, Vélizy-Villacoublay, France, 2014.
[31] T. Yu, J.G. Teng, Y.L. Wong, S.L. Dong, Finite element modeling of confined concrete-II: plastic-damage model, Eng. Struct. 32 (2010) 680–691, https://doi.org/10.1016/j.engstruct.2009.11.013.
[32] ACI, Building code requirements for structural concrete and commentary, ACI 318-4, 2014.

[33] J. Xiao, H. Liu, T. Ding, Finite element analysis on the anisotropic behavior of 3D printed concrete under compression and flexure, Addit. Manuf. 39 (2021), 101712, https://doi.org/10.1016/j.addma.2020.101712.
[34] GOM GmbH: Digital Image Correlation and Strain Computation Basics – Technical White Paper, 2018. ⟨https://www.gom.com/en/products/3d-testing⟩, (Accessed 27 January 2022).
[35] S. Chaves Figueiredo, C. Romero Rodríguez, Z.Y. Ahmed, D.H. Bos, Y. Xu, T.M. Salet, O. Çopuroğlu, E. Schlangen, F.P. Bos, Mechanical behavior of printed strain hardening cementitious composites, Materials 13 (2020), https://doi.org/10.3390/ma13102253.